Astron. Astrophys. 363, 253–268 (2000)

ASTRONOMY AND ASTROPHYSICS

The ISO-LWS map of the Serpens cloud core

I. The SEDs of the IR/SMM sources*

B. Larsson[1], **R. Liseau**[1], **A.B. Men'shchikov**[1], **G. Olofsson**[1], **E. Caux**[2], **C. Ceccarelli**[3], **D. Lorenzetti**[4], **S. Molinari**[5], **B. Nisini**[4], **L. Nordh**[1], **P. Saraceno**[6], **F. Sibille**[7], **L. Spinoglio**[6], **and G.J. White**[1,8,9]

[1] Stockholm Observatory, 133 36 Saltsjöbaden, Sweden (bem@astro.su.se)
[2] CESR CNRS-UPS, B.P. 4346, 31028 Toulouse Cedex 04, France
[3] Observatoire Grenoble, 414 rue de la Piscine, B.P. 53X, 38041 Grenoble Cedex, France
[4] Osservatorio Astronomico di Roma, Via Osservatorio 2, 00040 Monteporzio, Italy
[5] IPAC/Caltech, MS 100-22, Pasadena, California, USA
[6] Istituto di Fisica dello Spazio Interplanetario CNR, Tor Vergata, Via Fosso del Cavaliere, 00133 Roma, Italy
[7] Observatoire de Lyon, 69230 St. Genis-Laval, France
[8] Queen Mary and Westfield College, Department of Physics, University of London, Mile End Road, London E1-4NS, UK
[9] Astrophysics Group, The Cavendish Laboratory, University of Cambridge, Madingly Road, Cambridge CB3 OHE, UK

Received 6 March 2000 / Accepted 14 July 2000

Abstract. ISO-LWS mapping observations of the Serpens molecular cloud core are presented. The spectral range is $50 - 200\,\mu$m and the map size is $8' \times 8'$. These observations suffer from severe source confusion at FIR wavelengths and we employ a *Maximum Likelihood Method* for the spectro-spatial deconvolution. The strong and fairly isolated source SMM 1/FIRS 1 presented a test case, whose modelled spectral energy distribution (SED), within observational errors, is identical to the *observed* one. The model results for the other infrared and submillimetre sources are therefore likely to represent their correct SEDs. Simulations demonstrating the reliability and potential of the developed method support this view.

It is found that some sources do not exhibit significant FIR emission and others are most likely not pointlike at long wavelengths. In contrast, the SEDs of a number of SMMs are well fit by modified single-temperature blackbodies over the entire accessible spectral range. For the majority of sources the peak of the SEDs is found within the spectral range of the LWS and derived temperatures are generally higher (≥ 30 K) than have been found by earlier deconvolution attempts using IRAS data. SMM sizes are found to be only a few arcsec in diameter. In addition, the SMMs are generally optically thick even at LWS wavelengths, i.e. estimated $\lambda(\tau = 1)$ are in the range 160–270 μm.

The Rayleigh-Jeans tails are less steep than expected for optically thin dust emission. This indicates that the SMMs are optically thick out to longer wavelengths than previously assumed, an assertion confirmed by self-consistent radiative transfer calculations. Models were calculated for five sources, for which sufficient data were available, viz. SMM 1, 2, 3, 4 and 9. These models are optically thick out to millimetre wavelengths (wavelength of unit optical depth 900 to 1 400 μm). Envelope masses for these SMMs are in the range 2–6 $M_{\odot}$, which is of course considerably more massive than estimates based on the optically thin assumption. The luminosities are in the range 10–70 $L_{\odot}$, suggesting the formation of low-mass to intermediate mass stars, so that the existence of such massive envelopes argues for extreme youth of the SMMs in the Serpens cloud core.

Finally, we present, for the first time, the full infrared SEDs for the outburst source DEOS, both at high and low intensity states.

Key words: ISM: individual objects: Serpens cloud core – ISM: clouds – ISM: general – ISM: dust, extinction – stars: formation

1. Introduction

The Serpens molecular cloud is a magnificent laboratory for the study of multiple low mass star formation. The cloud core has a high density of young stellar objects (YSOs), including several submillimetre sources: for a distance of 260 pc, Kaas (1999) estimated a surface density of 400–800 YSOs per square parsec, which is several times higher than found in the star forming western parts of the ρ Oph clouds (~ 100 pc^{-2}, Bontemps et al. 2000 and references therein). The extremely high visual extinction makes the Serpens cloud core nearly exclusively accessible to infrared and sub-/millimetre observations (e.g., Casali et al. 1993, Hurt & Barsony 1996, Davis et al. 1999). The submillimetre sources, named SMM by Casali et al. (1993), are distributed in a southeast-northwest direction with a concentration of sources in two clusters. This is also true for the presumably

Send offprint requests to: B. Larsson (bem@astro.su.se)

* Based on observations with ISO, an ESA project with instruments funded by ESA Member States (especially the PI countries: France, Germany, the Netherlands and the United Kingdom) and with the participation of ISAS and NASA.

Table 1. ISO observations of the Serpens cloud core

Target Name	Principal Investigator	Mode†	Offsets‡ (″) R.A.	Dec.	Date
LWS					
Map	R. Liseau	L01	0	0	21-Oct-96
Flow	P. Saraceno	L01	0	−33	23-Oct-97
Field	P. Saraceno	L01	−100	50	08-Mar-97
Field	P. Saraceno	L01	100	50	08-Mar-97
SMM2	M. Spaans	L02	151	−148	14-Apr-96
SMM3	M. Griffin	L01	140	−78	21-Oct-96
SMM4	M. Griffin	L01	101	−124	21-Oct-96
S68N	M. Spaans	L02	−32	95	14-Apr-96
SWS					
DEOS	T. Prusti	S01	−18	61	14-Apr-96
DEOS	T. Prusti	S01	−18	61	01-Sep-96
DEOS	T. Prusti	S01	−18	61	24-Oct-96
DEOS	T. Prusti	S01	−18	61	08-Mar-97
DEOS	T. Prusti	S01	−18	61	12-Apr-97
DEOS	T. Prusti	S01	−18	61	22-Sep-97
CAM					
Serp B	M. Casali	CVF	128	−54	14-Apr-96
S68N	P. André	CVF	24	31	14-Apr-96
DEOS	G. Olofsson	LW2	−18	61	14-Apr-96
DEOS	G. Olofsson	LW3	−18	61	14-Apr-96
DEOS	T. Prusti	LW2	−18	61	22-Sep-97
DEOS	T. Prusti	LW3	−18	61	22-Sep-97

† Instrumental modes: L01 and S01 refer to the full wavelength range of the LWS and SWS, respectively. L02 stands for LWS line spectrum scans. CVF denotes spectrum imaging with the Continuous Variable Filter of ISOCAM. LW2 and LW3 are two broad band ISOCAM filters centered at 6.7 and 14.3 μm respectively.
‡ Offsets are relative to the centre coordinates of the LWS map, viz. R.A. = $18^{\rm h}29^{\rm m}50\overset{\rm s}{.}29$ and Dec. = $1^\circ\ 15'\ 18\overset{\prime\prime}{.}6$, J 2000.

more evolved objects (Class I and II, see: Kaas 1999). The region also includes a great number of Herbig-Haro objects and molecular flows, where at least some can be connected with SMMs (e.g., Ziener & Eislöffel 1999, McMullin et al. 1994, White et al. 1995, Curiel et al. 1996). Outflows are seen to accompany star formation at all observed evolutionary stages.

Submillimetre sources are often found in dense molecular cloud cores and are believed to identify birth places of stars. For the Serpens sources, Hurt & Barsony (1996) used image sharpening techniques to analyse low resolution, broadband IRAS data. Cores in low mass star forming regions are generally thought to be cold, with temperatures of about 20 K or below. Emission from such objects will peak at wavelengths typically longer than 100 μm, which makes the Long Wavelength Spectrometer (LWS) on board the Infrared Space Observatory (ISO) an instrument more suited than IRAS to study these sources. In addition, the LWS provides two orders of magnitude higher spectral resolution over its spectral range of 50 to 200 μm.

The LWS observations presented in this paper aim to address the nature and evolutionary status of the SMMs in the Serpens cloud core, in particular their physical state (T, ρ, M, L etc.). The observables to be discussed are the spectral energy distributions of these objects, obtained over a broad spectral range. This paper utilises mapping observations of the Serpens cloud core with the LWS and complementary observations, including pointed LWS data and observations with other instruments aboard ISO. In Sect. 2, an account of these observations ($8' \times 8'$ map and ISO archive retrievals) and their reduction is given, and the results are presented in Sect. 3. The ISO-LWS map is highly undersampled and in Sect. 4, we introduce a *Maximum Likelihood Method* for the extraction of the SEDs of the spatially confused submm sources. The discussion focusses on the comparison of conventionally applied analysis methods (single temperature, optically thin approximation) with that based on the detailed and self-consistent modelling of the radative transfer. Finally, in Sect. 5, the main conclusions of this work are briefly summarised.

2. Observations and data reductions

2.1. The ISO observations

A grid of 25 positions of FIR-spectra in the Serpens cloud core was obtained with the Long-Wavelength Spectrometer (LWS; 43–197 μm, $R_\lambda = 140 - 330$) on board the Infrared Space Observatory (ISO) on October 21, 1996. An account of the ISO-project is given by Kessler et al. (1996). The LWS is described by Clegg et al. (1996) and Swinyard et al. (1996).

The formal map centre, viz. $\alpha = 18^{\rm h}29^{\rm m}50\overset{\rm s}{.}29$ and $\delta = 1^\circ\ 15'\ 18\overset{\prime\prime}{.}6$, epoch J 2000, coincides to within $10''$ with the position of the sub-millimetre source SMM 1. The pointing accuracy in the map is determined as $1''$ (rms). The spacings between positions in the map, oriented along the coordinate axes, are $100''$ in both Right Ascension and Declination. These offsets correspond to the pre-flight estimates of the circular LWS-beam, HPBW. The actual beam widths are however smaller, $70''$ to $80''$, leading to appreciable spatial undersampling. This is also evident in Fig. 1, where the LWS-beams and pointings are represented by circles. The size of the 5×5 LWS-map is thus $8' \times 8'$, corresponding to $(0.7 \times 0.7 = 0.5)\, D_{310}^2$ pc^2, where D_{310} denotes the distance to the Serpens cloud core in units of the adopted value of 310 pc (de Lara et al. 1991).

At each map-point the grating of the LWS was scanned 6 times in fast mode, oversampling the spectral resolution by a factor of 4. Each position was observed for nearly 15 min. The centre position was re-observed half a year later on April 15, 1997, for a considerably longer integration time (24 spectral scans; Larsson et al. in prep.). The internal agreement between the deep integration and the map spectrum is excellent, giving confidence that the rest of the map data is also of good quality.

Our map spectra were complemented with LWS spectra at 7 positions inside the mapped area, which were retrieved from the ISO-archive (Table 1). In addition, 1D-spectral observations with the Short-Wavelength Spectrometer (de Graauw et al. 1996: SWS; FOV = $14'' \times 20''$ to $17'' \times 40''$, 2.4–45 μm, $R_\lambda \sim 10^2$–10^3) and imaging spectrophotometry with the Continuous Variable Filter (CVF; 2.5–15.5 μm, pixel-FOV = $6''$,

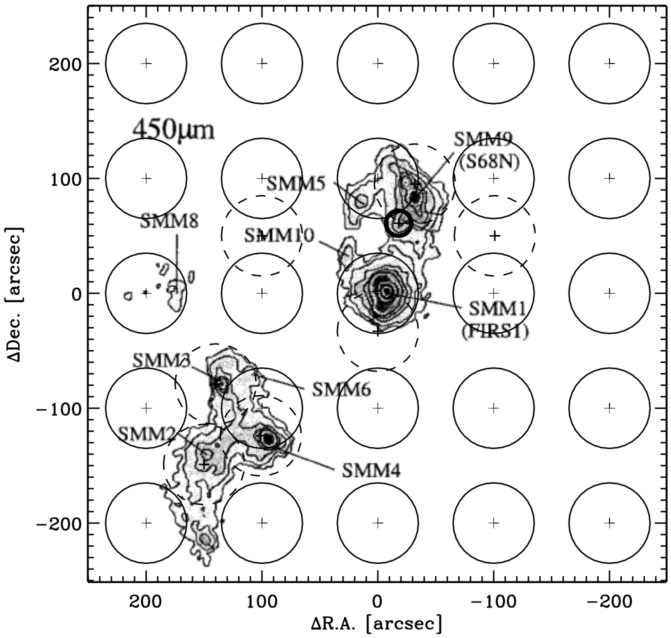

Fig. 1. Outline of the $8' \times 8'$ map of the LWS observations, shown together with the 450 μm continuum map of Davis et al. (1999). Conventional source names are indicated. Solid circles about grid-points and broken circles about other map-points (see Table 1) outline the contours of the HPBW of the LWS, taken as $70''$. The small symbol south of SMM9 identifies the pointing of the SWS, the aperture of which is rectangular $14'' \times 20''$ to $17'' \times 40''$ depending on the wavelength. The LWS-map is centred on the far-infrared/sub-millimetre source FIRS 1/SMM 1 and the offsets of $100''$ in both Right Ascension and Declination (plus signs) correspond to the pre-flight estimates of the LWS-beam

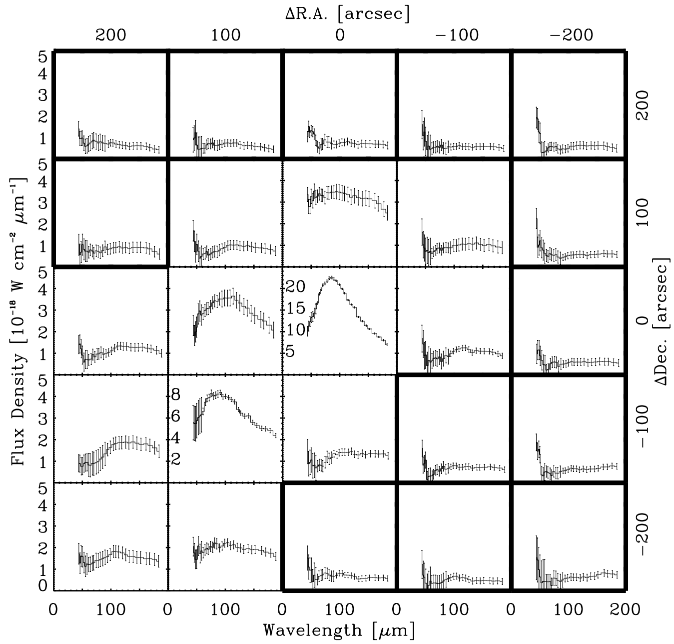

Fig. 2. 50–200 μm spectra towards the grid points of the LWS-map. The spatial offsets are given along the upper and right-hand axes. The wavelength scale is found along the lower axes and that of the flux density along the left-hand axes, except for (0$''$, 0$''$) and (–100$''$, –100$''$), for which the scale is given inside the sub-frames. The LWS data have been rebinned to the spectral resolution $R_\lambda = 20$. The error bars reflect the differences of the displayed median data (solid line) and the original data, prior to the detector stitching. The FIR-background spectrum is defined as the straight average of the spectra inside the boxes with the thick lines

$R_\lambda \gtrsim 35$) of ISOCAM (Cesarsky et al. 1996) were also analysed. Further, broadband ISOCAM images at 6.7 and 14.3 μm and with pixel-FOV both 1$''$.5 and 3$''$ were part of the observational material.

In summary, Table 1 provides an overview of the observational material employed in this paper. Fig. 1 shows the SWS and LWS pointing positions superposed onto the sub-millimetre continuum map (450 μm) of Davis et al. (1999), where 9 discrete sub-millimetre sources (SMM 1 – SMM 10, except SMM 7) are identified.

2.2. The reduction of the ISO data

The LWS observations were pipeline-processed (OLP 7.1) and were subsequently reduced with the interactive analysis package LIA. Post-pipeline processing of the SWS and LWS data was done with the package ISAP and of the ISOCAM data with the corresponding CIA programs.

At each position, the individual LWS scans for each of the 10 detectors were examined, 'deglitched' and averaged. Corrections were applied to the 'fringed' spectra in the map. The fringing indicates that the emission is extended and/or that point sources were not on the optical axis of the LWS, i.e. the radial distance from the optical axis was larger than about 25$''$.

For the LWS data we believe that the absolute flux calibration is good to an accuracy of 30% (Swinyard et al. 1996), whereas relative offsets between overlapping spectral regions of adjacent detectors were generally within 10% ('detector stitching' uncertainty, see also Fig. 2). Internally, the LWS-accuracy is much higher than 30% for the Serpens cloud core, as is evidenced by observations of the same targets at different times and under different observing conditions (e.g., pointed vs. mapping observations).

The absolute accuracy could be less, however, in the very weak spectra towards the northern and western edges of the map, for which the flux uncertainties are dominated by the dark current correction. This was estimated based on measurements directly before and after, but not during, the mapping observations. Suspected dark current drifts during the observation of the first 5 map points, viz. from (–200$''$, –200$''$) to (–200$''$, 200$''$), were however approximatively linear in time, whereas for the remaining spectra, the dark current seemed to have stabilised at a constant value. Support for our applied dark current corrections is provided by the fact that these resulted in fluxes which are in very good agreement with IRAS-ISSA data at 60 and 100 μm (formally within 7% and 4%, respectively, see: Fig. 4).

The reduction of the SWS data is similar to that of the LWS data, whereas the reduction of the CVF data involved additional corrections for transients and flat field.

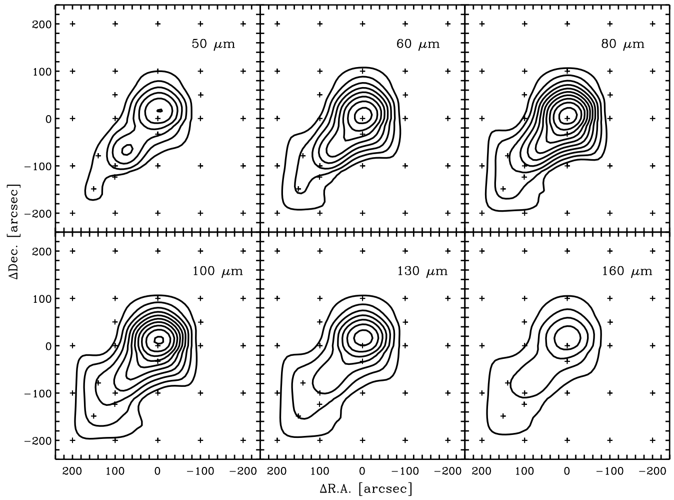

Fig. 3. Spatial distribution of the continuum emission in the LWS-map in wavebands centred on 50, 60, 80, 100, 130 and 160 μm, with spectral bandwidth of 10 μm. Contours are spaced by $2\,10^{-17}$ W cm^{-2}, the lowest contour is at $2\,10^{-17}$ W cm^{-2} and the displayed dynamic range is a factor of 10

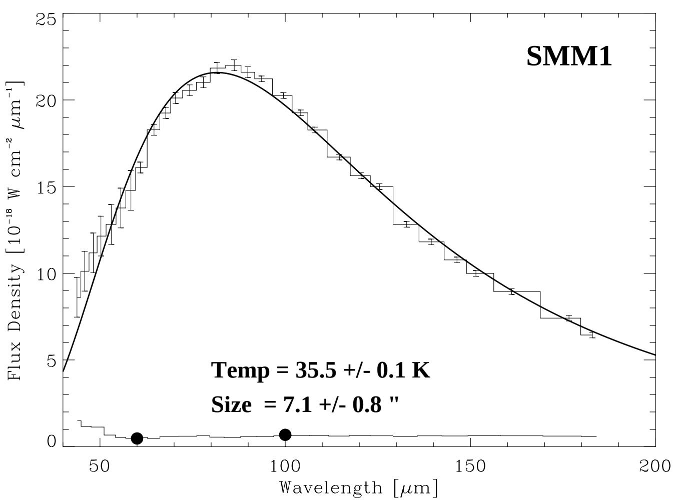

Fig. 4. A pure blackbody fit ($\beta = 0$, see the text) to LWS data of SMM 1 results in the indicated values of the temperature and diameter of a circular source, the formal errors of which are given as the standard deviation about the best-fit values (χ^2-minimisation). The displayed LWS spectrum has been re-binned to a resolution of 20. The displayed error bars correspond to the relative flux uncertainty, when stitching together the 10 individual detectors of the LWS. At the bottom of the figure, the (subtracted) average background spectrum is shown for reference and compared to IRAS data (filled circles)

3. Results

From Fig. 2 it can be seen that detectable FIR emission is present at all observed positions. The sensitivity of these map data at long LWS wavelenghts is of the order of 10^{-19} W cm^{-2} μm^{-1} (about 3 Jy per beam at 100 μm), whereas this noise level becomes worse by a factor of about two towards the shorter wavelengths.

As pointed out in Sect. 2.2, most of the observed spectra were fringed. The situation is different at the map centre, where the LWS spectrum shows hardly any fringes at all. This strongly suggests that the FIR-emission is dominated by a source which is pointlike to the LWS and which was reasonably well centred in the aperture during the observation. As is also evident from Fig. 3, where LWS measurements in 6 continuum bands between 45 μm and 165 μm are presented, that this source dominates the emission at all FIR wavelengths. In the following section, the physical characteristics of this source will be discussed.

4. Discussion

4.1. The sub-millimetre source SMM 1

4.1.1. The blackbody observed by the LWS

The centre position of the map dominates the emission over the entire wavelength range of the LWS (Fig. 3). This map point coincides with the strong sub-millimetre source SMM 1/FIRS 1. At FIR and sub-mm wavelengths, this source is relativly isolated. Any problem of source confusion is therefore very much reduced in this case.

As evident in Fig. 4, the FIR spectrum is well fit by a single blackbody of temperature 36 K. Such a relatively high temperature was also determined by, e.g., Nordh et al. (1982), Harvey et al. (1984), McMullin et al. (1994) and Davis et al. (1999). The diameter of the hypothetically circular source is $\sim 7''$, i.e. $(2\,200 \pm 250)\ D_{310}$ AU. This latter value confirms the point-like nature of the far-infrared source, as was suspected in the previous section on the basis of its largely unfringed spectrum. It is also comparable to the source sizes seen in the interferometric observations at millimetre wavelengths by Hogerheijde et al. (1999). In contrast, the temperature derived here is significantly higher than the 27 K obtained by Hurt & Barsony (1996) from high resolution IRAS data (HIRES).

4.1.2. A modified blackbody fit to the SED of SMM 1

In Fig. 5, the LWS spectrum is shown together with data collected from the literature. From this overall Spectral Energy Distribution (SED) it is clear that the LWS data are sufficient to determine the luminosity of the source. However, it is also apparent that at longer wavelengths the SED is steeper than the Rayleigh-Jeans fall-off of the blackbody ($\lambda\,F_\lambda \propto \lambda^{-3}$), which could indicate that the emission is becoming optically thin somewhere outside the spectral range of the LWS. Provided that in this optically thin regime the dust opacity follows a power law, viz. $\kappa_\lambda \propto \lambda^{-\beta}$, this index β can be determined from the observations, since then $\lambda\,F_\lambda \propto \lambda^{-(3+\beta)}$ as $\lambda \rightarrow \infty$ for any density and/or temperature structure of the envelope (spherical symmetry and central radiating source). A least squares fit to the data between 0.8 mm and 3.4 mm yields $\beta_{\rm obs} = -\left(\frac{d\log\lambda F_\lambda}{d\log\lambda} + 3\right) = 1.2 \pm 0.2$. At these relatively long wavelengths, this statistical error is considerably larger than any deviation of the modified Rayleigh-Jeans law from the (modified) Planck curve, viz. $F_\lambda({\rm Planck})/F_\lambda({\rm RJ}) = \left(1.44 \times 10^4/\lambda_{\mu{\rm m}}\,T\right) / \left[\exp\left(1.44 \times 10^4/\lambda_{\mu{\rm m}}\,T\right) - 1\right]$, which

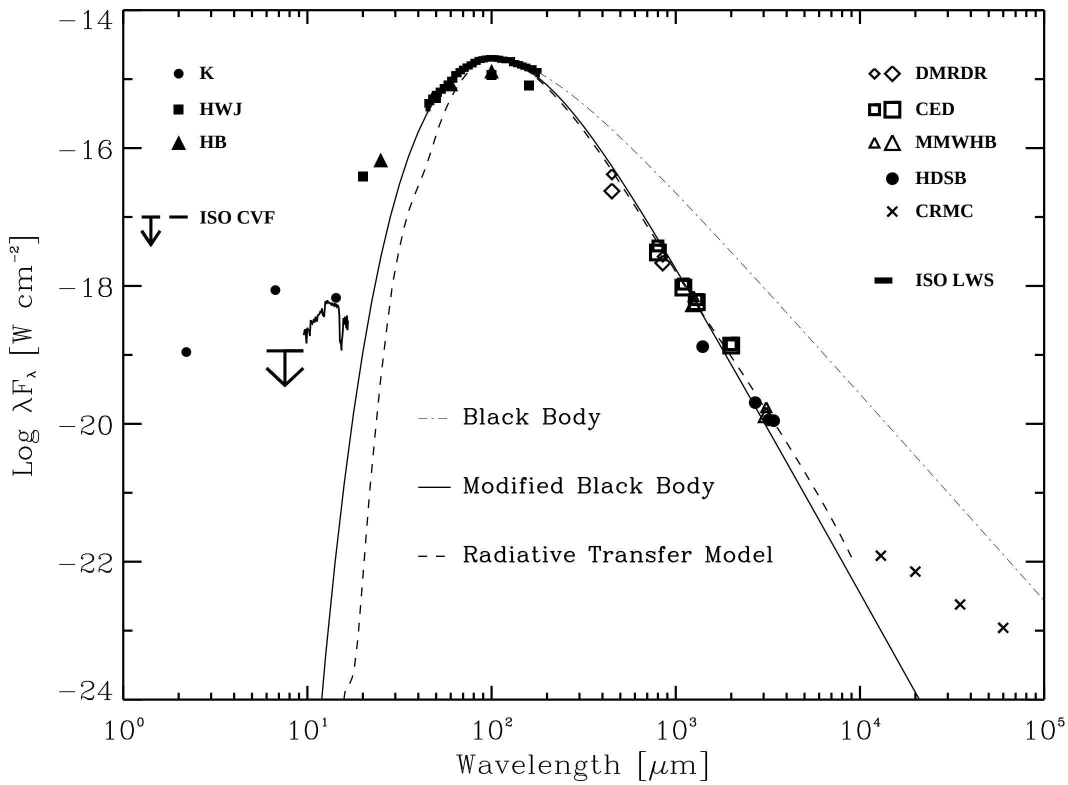

Fig. 5. The SED ($\lambda\, F_\lambda$ vs λ) of SMM 1, between 2 μm and 6 cm. Open symbols identify data which have been obtained with apertures larger than 7$''$, with the small open symbols indicating the according to Eq. (3) beam-matched data. The thin solid line shows a conventional (modified blackbody) fit to these data within 40 μm $\lesssim \lambda \lesssim$ 3 mm and, for reference, the 36 K-blackbody of Fig. 4 is shown by the dash-dot line. The dashed line depicts the SED obtained from a model, for which the radiative transfer through the dust envelope is treated self-consistently. The line thickness for the LWS and CVF data, respectively, are shown in the legends inside the figure. The accompanying upper limit symbol refers to the short-wave CVF data. The photometric data collected from the literature are referenced to as K = Kaas (1999), HWJ = Harvey et al. (1984), HB = Hurt & Barsony (1996), DMRDR = Davis et al. (1999), CED = Casali et al. (1993), MMWHB = McMullin et al. (1994), HDSB = Hogerheijde et al. (1999), CRMC = Curiel et al. (1993). The near-infrared data ($\lambda \lesssim 10\,\mu$m) are probably unrelated to SMM 1 (see: the text)

for $T = 36$ K would result in the "correction" of $\beta_{\rm obs}$ by -0.087.

Following standard procedures (e.g. Hildebrand 1983, Emerson 1988), we can then estimate the envelope mass. Using only the data between 40 μm and 3 mm, which were collected with sufficiently large telescope beams, i.e. larger than 7$''$ and shown as open symbols in Fig. 5, a modified blackbody can be fit to this section of the SED for a single temperature. Hence, the flux density is given by

$$F_\lambda = \left(1\,-\,e^{-\tau_\lambda}\right)\,\Omega_{\lambda,\,S}\,B_\lambda\,(T) \tag{1}$$

with obvious notations. In this wavelength regime, the opacities of dust grains generally display power law dependencies (e.g., Ossenkopf & Henning 1994). Hence, let the continuum optical depth scale as

$$\tau_\lambda = \tau_{\lambda,\,0}\left(\frac{\lambda_0}{\lambda}\right)^{\beta} \tag{2}$$

A first order correction for the finite beam sizes to the flux density (shown as small open symbols in Fig. 5) was included by

$$F_\lambda = \frac{\Omega_{\lambda,\,\rm LWS}}{\Omega_{\lambda,\,B}}\left(\frac{\Omega_{\lambda,\,S}+\Omega_{\lambda,\,B}}{\Omega_{\lambda,\,S}+\Omega_{\lambda,\,\rm LWS}}\right)\,F_{\lambda,\,B} \tag{3}$$

where $\Omega_{\lambda,\,\rm LWS}$ is the beam size of the LWS at different wavelengths, λ (see Sect. 4.2.1 and Fig. 9), $\Omega_{\lambda,\,B}$ is the beam size of the telescope in question, $\Omega_{\lambda,\,S}$ is the source size, and $F_{\lambda,\,B}$ is the source flux reported in the literature. Any dependence of the source size on the wavelength is naturally accounted for by the radiative transfer modelling of Sect. 4.1.3. Here, it is assumed that the source size is the same as that of the blackbody fit and constant with wavelength.

This modified blackbody remains optically thick far beyond 100 μm, up to $\lambda(\tau=1) = 250\,\mu$m, the wavelength of unit optical depth. Longward of this wavelength the emission is optically thin and the total column density, $N(\rm H_2)$, can be estimated from

$$\tau_\lambda = \int \kappa_\lambda\,\rho(\ell)\,d\ell = \kappa_\lambda\,\mu\,m_{\rm H}\,N({\rm H_2})\,\left(\frac{M_{\rm gas}}{M_{\rm dust}}\right)^{-1} \tag{4}$$

so that

$$N({\rm H_2}) = \int n_{\rm H_2}(\ell)\,d\ell = \frac{\tau_{\lambda_0}}{\kappa_{\lambda_0}\,\mu\,m_{\rm H}}\,\frac{M_{\rm gas}}{M_{\rm dust}} \tag{5}$$

Taking $\kappa_{\lambda_0} = 1\,{\rm cm^2\,g^{-1}}$ at $\lambda_0 = 1.3$ mm (Ossenkopf & Henning 1994) and $\tau_{\lambda_0} = 0.05$, $\mu = 2.4$ for molecular gas and

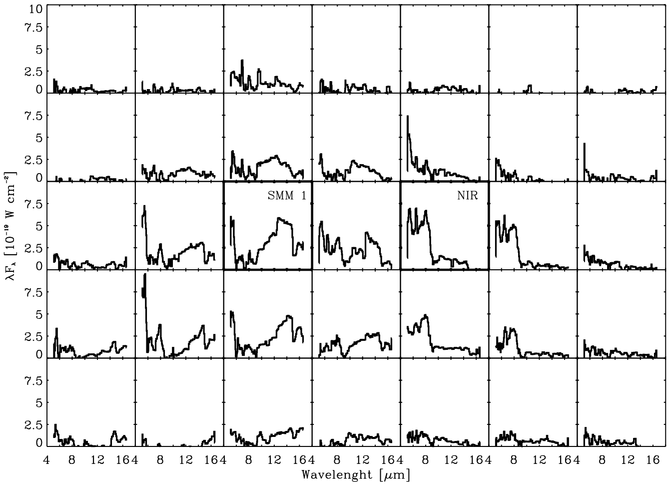

Fig. 6. CVF view of the 5 to 15 μm SED towards SMM 1 inside the LWS beam. The pixel size is 6″, hence the shown map is 42″ × 30″. The map orientation is offset from the axes of the equatorial system, rotated at a negative position angle of a few degrees. Note the clear difference between the SED of the NIR object (distinctly 'blue') and that of SMM 1 (distinctly 'red') close to the map centre and separated by less than 20″

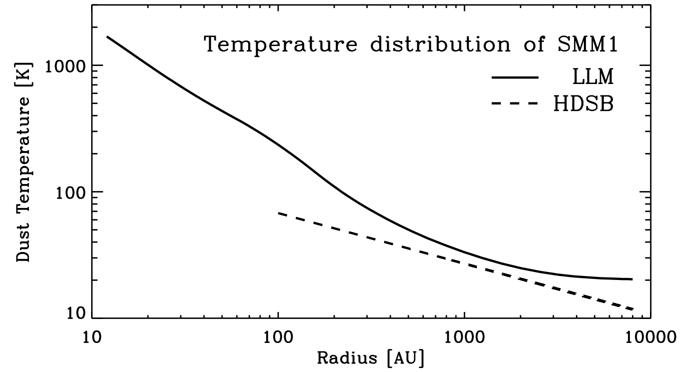

Fig. 7. The radial run of the temperature in the (assumed) spherical envelope of SMM 1. The solid line shows the optically thick dust envelope, obtained from the self-consistent radiative transfer model discussed in the text (LLM = this paper). For comparison, the optically thin model with $T \propto r^{-0.4}$ by Hogerheijde et al. (1999), and identified as HDSB, is shown by the dashed line. Both models assume an r^{-2} density law and the same grain opacities. When compared to the optically thin assumption, the run of the temperature is markedly different: a considerably steeper gradient is needed in most regions of the envelope to drive out the centrally generated flux ($\sim$ 70 $L_\odot$)

the gas-to-dust mass ratio $M_{\rm gas}/M_{\rm dust} = 10^2$, the average column density is $N(H_2) = 1.3\,10^{24}$ cm^{-2}. For the assumed source radius of 1100 AU, the mass of the optically thin envelope of SMM 1 is 2.2 D_{310}^2 $M_\odot$. The average volume density $n(H_2)$ corresponds then to several times 10^7 cm^{-3}, which is consistent with our choice of the theoretical opacities for grains with thin ice mantles for dense protostellar regions. However, the observationally determined value of β seems only marginally compatible with the opacity law, for which $\beta = 1.8$. If one accepts that the opacities are generally correct per se, the observed low β values (see also Table 2) could indicate that the optical depth through the dust has been under-estimated even at long wavelengths.

The assumption of an isothermal, homogeneous sphere is of course very crude and physically not at all compelling. However, the LWS data do not contain any information which can constrain the structure of the source. Hogerheijde et al. (1999), on the other hand, found evidence for structure in the visibility curves of their mm-wave data and adopted a radial power law distribution for the density, $n(r) \propto r^p$ with $p \sim -2$, so that their model of SMM 1 is more centrally condensed. For a spherical, centrally heated optically thin dust envelope, a power law is also expected for the temperature profile, viz. $T(r) \propto r^q$. The exponent is in this case given by $q = -2/(4+\beta)$, where β refers as before to the wavelength dependence of the absorption cross section of the dust grains. Since $\beta_{\rm obs} \sim 1$, the temperature profile could be expected to exhibit $q \sim -0.4$, a value which was indeed also used by Hogerheijde et al. (1999).

It has been suggested that SMM 1 is a so called Class 0 source (André et al. 1993) and the correct assessment of its envelope mass (and central mass, of course) is of particular importance for such type of object. In the following section, we shall attempt to improve on the reliability of the parameters for SMM 1 by treating the radiative transfer through the dust envelope in a self-consistent manner.

Before doing that, we need to address the possible near-infrared excess over a Class 0 SED, however (see Fig. 5). It is clear that over the 7″ source size, the deduced column density, $N(H_2) = 10^{24}$ cm^{-2}, would imply an accompanying visual extinction of $A_V \sim 10^3$ mag (Bohlin et al. 1978, Savage & Mathis 1979), or still nearly $A_K \sim 100$ mag at 2 μm (Rieke & Lebofsky 1985). Therefore, on arcsecond scales around SMM 1 one would hardly expect any detectable direct flux in the near-infrared. This assertion is confirmed by ISOCAM-CVF observations (Table 1) which show that the NIR flux originates from a source different from SMM 1. In Fig. 6, a map of the spectra on the 6″ pixel scale are shown. Obviously, SMM 1 and the source west of it do not have the same SEDs in the 3 to 15 μm region. Hence, we conclude that the SED of SMM 1 contains less NIR flux than indicated in Fig. 5 and, consequently, these observations are supporting the view that SMM 1 is indeed a Class 0 object.

4.1.3. Self-consistent radiative transfer models of SMM 1

The models by Hogerheijde et al. (1999) are based on the assumption of optically thin emission. However, it was realised in the previous section that optical depth effects might affect the SED of SMM 1 even at long wavelengths. In order to test this hypothesis we have run models of the transfer of radiation through the dust envelope of the source. A fuller description of these computations will be presented in a forthcoming paper (Larsson et al. in prep.). From the comparison with the observations, these self-consistent models provide the temperature distribution in the envelope. For instance, Fig. 7 depicts the true temperature profile of the Hogerheijde et al. model of SMM 1

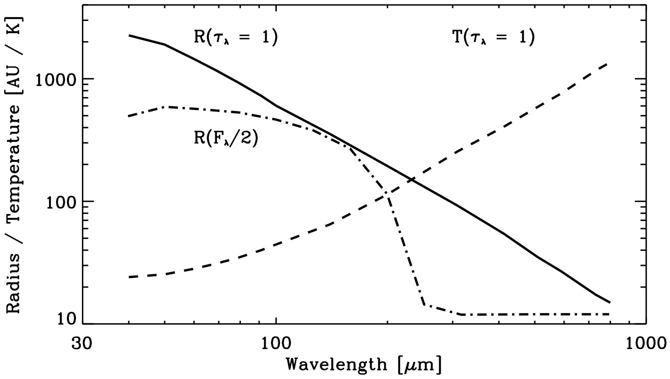

Fig. 8. Surfaces of unit optical depth of the model of SMM 1 in the far infrared and sub-millimetre (40 μm to about 1 mm). Shown is the variation of the source size with wavelength, i.e. the radius, $R(\tau_\lambda = 1)$ in AU, and the corresponding dust temperature at this radial distance from the central heating source, $T(\tau_\lambda = 1)$ in K. The dash-dotted line, labelled $R(F_\lambda/2)$, designates the locus of the radius at which half of the flux at a given wavelength is emitted

(see below). For the general cloud background we estimate a temperature of 20 K, and that flux has been subtracted from the model of SMM 1.

Complying with Hogerheijde et al. (1999), we adopt a spherically symmetric geometry of the dust envelope about a central heating source and a radial power law distribution for the density, with $p = -2$ (in order to reproduce the visibilites obtained by these authors), i.e. $n(r) = 1.7 \times 10^{11}\ (r/12\ \mathrm{AU})^{-2}\ \mathrm{cm}^{-3}$, which reproduces the density at 100 AU we inferred from that paper. As before, the opacities were taken from Ossenkopf & Henning (1994), specifically the model identified as *MRN with thin ice mantles, density* 10^7 cm^{-3} *and age* 10^5 yr (although one would not expect these thin ice mantles to survive in the central regions of the envelope, where temperatures are greately in excess of 100 K, we kept this particular choice of opacities for comparison with the other models; using other grain compositions did not change the *general* results).

The model reproduces indeed the visibilites of SMM 1. Further, the observed SED is reasonably well fit at long wavelengths (Fig. 5), i.e. the observed β-value is obviously reproduced. This is mainly because the envelope is optically thick out to nearly 1 mm ($\lambda_{\tau=1} = 900\,\mu$m, see the Tables 2 and 3, where also other model results are provided). As expected, the "blackbody parameters" of the model are not vastly different from the single temperature fit: e.g., the diameter and temperature of the spherical source are $4''$ and 43 K, respectively, for unit optical depth at 100 μm, viz. for $\tau_{100\,\mu\mathrm{m}} = 1$. Values at other wavelengths are presented graphically in Fig. 8. Evidently, at the longer wavelengths, one 'looks' progressively deeper into the envelope, towards hotter and denser regions. Further, at the longer wavelenghts more than half of the flux originates from the inner regions, where the dust destruction front is located. This is shown in the figure as $R(F_\lambda/2)$, i.e. the radius at which half of the flux at a given wavelength is emitted.

We shall not dwell further on the details of these specific radiative transfer calculations, for the following reason: although the model fit is quite acceptable in the FIR and submm/mm spectral region, it clearly underproduces the flux at wavelengths shortward of the peak of the SED (Fig. 5). The remedy of this shortcoming requires the relaxation of the assumption regarding the source geometry. Because of disk formation, spherical geometry is generally not considered a good approximation for YSOs, including protostellar objects. It is possible, in fact, to satisfactorily fit the entire SED using a radiative transfer model in a 2d axially symmetric geometry (disk plus envelope). The results of such computations will be presented in a follow-up paper (Larsson et al. in prep.).

4.2. The other SMMs of the Serpens cloud core

In Fig. 3, a secondary emission peak lies on the extension towards the south-east. This morphology is very similar to that previously seen at FIR wavelengths (e.g., Nordh et al. 1982, Harvey et al. 1984, Hurt & Barsony 1996) and also at longer wavelengths (Casali et al. 1993, Testi & Sargent 1998, Davis et al. 1999). In particular at higher spatial resolution, this emission region breakes up into numerous point-like sources. Because of this source crowding, severe source confusion within the LWS-beam can be expected at FIR wavelengths. In the next section, we shall attempt to disentangle the various contributions from the different sources. This is possible, because spatially filling-in and overlapping LWS data are in existance (see Table 1 and Fig. 10).

4.2.1. SEDs of confused sources: spectro-spatial deconvolution of the LWS data

To search for the FIR sources and to deduce their associated SEDs we developed a program for a *Maximum Likelihood Method* (e.g., Lucy 1974) and applied it to the entire set of LWS-map data (Table 1).

The first of two basic assumptions is that all sources are point-like, which is probably reasonable considering the large beam size of the LWS (HPBW $\sim 70''$). In support of this, SMM 1 was found, in the previous sections, to be a point source. Secondly, the exact positions of all sources are assumed known and kept fixed. These were taken from ISOCAM observations in the mid-infrared (Kaas 1999) and/or from observations in the submillimetre by Davis et al. (1999). We then pick an arbitary grid point within the field of the LWS-map and try to estimate, at that location and for a fixed frequency, the radiative flux which originated from all sources in the field. This is done at all locations and for all LWS wavelengths in an iterative scheme as described in more detail in Appendix A.

For the restauration of the source spectra, the band-width corresponded always to the spectral resolution $R_\lambda = 20$. For the wavelength dependent beam pattern of the LWS, $\Omega_{m,s}$, the azimuthal averages of the presently best known values were used (see Fig. 9). This was done for all ten detectors of the LWS and out to $\sim 150''$ from the beam centre, which would

Table 2. Dust temperatures, sizes and opacity indices of IR/SMM envelopes in the Serpens cloud core

Source Name	$T_{\rm dust}$ (K)			⊘ (arcsec)			$\beta_{\rm obs}$			Note¶
	bb†	$\tau_{100\mu m}$=1†	HB	bb†	$\tau_{100\mu m}$=1†	HB	LLM§	DMRDR	CED	
SMM 1/FIRS 1	36	43	27	7 ± 1	4	12	1.2 ± 0.2	0.9	0.5 ± 0.2	
SMM 2	33:	36	24	3 ± 2:	1.5	20	0.2 ± 1.9	1.1	0.8 ± 0.8	1
SMM 3	31	32	24	5 ± 2	3	20	0.6 ± 0.2	0.8	-0.1 ± 0.4	
SMM 4	30	27	20	5 ± 2	4	20	0.8 ± 0.2	0.8	0.5 ± 0.3	
SMM 5/EC 53						20	0.9 ± 0.9	0.9	1.6 ± 0.5	1, 2, 3
SMM 6/SVS 20						20	0.5 ± 2.4	0.8	1.3 ± 1.0	1, 2, 3
SMM 8	21:			6 ± 3:						
SMM 9/S 68N	24	27	23	9 ± 4	3.5	20		1.2		
SMM 11/HB 1	31:			4 ± 2:						1, 3
HB 2	24:			5 ± 3:						
SVS 2	25:			9 ± 5:						1, 3

References: HB = Hurt & Barsony (1996), LLM = this paper, DMRDR = Davis et al. (1999), CED = Casali et al. (1993).
¶ 1 = extended emission, 2 = excluded from calculation, 3 = near infrared source (see the text).
† Temperature and diameter values are for bb = blackbody fit and $\tau_{100\mu m} = 1$ refers to the radiative transfer model.
§ Our $\beta_{\rm obs}$ has been evaluated between 0.8 mm and 3.4 mm.

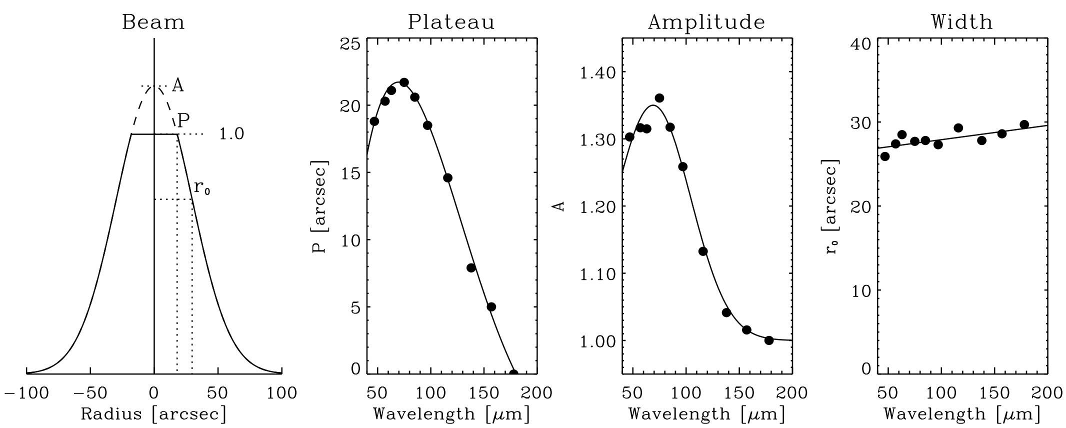

Fig. 9. The beam of the LWS at the centre wavelengths of its ten detectors (SW 1 to SW 5 and LW 1 to LW 5, see Clegg et al. 1996). Azimuthal averages are represented by the filled dots and the full lines refer to the continuous functions fitted to these data. For the distance r from the beam centre (optical axis) in arcsec we have $\Omega_\lambda(r) = 1$ if $r < P$ and $\Omega_\lambda(r) = A\,\exp[-\frac{1}{2}\,(\frac{r}{r_0})^2]$ if $r > P$, where the *plateau* P is shown in the second panel from the left, the *amplitude* A in the following panel and the *width* r_0 in the right hand panel. An explanatory sketch of this parameterisation is provided in the farmost left hand panel

correspond to about the 5% level of a perfectly Gaussian beam. The observational basis for this was raster mapping of the point-like planet Mars (B.M. Swinyard and C. Lloyd 1999, private communication).

In Fig. 10, the sources which were included in the modelling are identified and shown together with the pointings of the LWS. These sources are recognized as the strongest ones at sub-millimetre (SMM 1–11, except SMM 7 and 10) and/or at mid-infrared wavelengths (SVS 2, SVS 4 and SVS 20). The spectra were corrected for background emission, which was defined along the northern and western edges of the map (see Figs. 2 and 4). For these prominent sources, convergence was typically achieved after five iterations. In general, the computations were halted after visual inspection of the results, but tests were run up to 1000 iterations demonstrating that the solutions were stable. In Appendix B, a demonstration of the algorithm's reliability is provided using known source spectra. It is also gratifying to note that the procedure left, as could be expected, the spectrum of SMM 1 essentially unaltered, i.e. the *Maximum Likelihood Method* solution for this source is entirely within the quoted errors. Yet another check was provided by an LWS Guaranteed Time observation half a beamwidth south (labelled ‘Flow’ in Table 1), which was correctly recovered by our method. Since these observations were apart in time by 1 year, this result also indicates that no significant FIR-intensity variations have occurred on that timescale.

To properly appreciate the results to be presented below and summarised in Tables 2 and 3, it might be useful to remember that the method attempts to retrieve information which is hidden inside the spatial resolution of the observations. Therefore, these solutions represent, at best, very likely possibilities of what these source spectra might look like. Note that the 30

Table 3. Luminosities, opacities and masses of SMM envelopes in the Serpens cloud core

Source Name	$L^\dagger$ ($L_\odot$)			$\lambda^{\pounds}_{\tau=1}$ (μm)		$N(H_2)^\ddagger$	$M^\dagger_{\rm envelope}$ ($M_\odot$)				Note
	LLM	HB	CED	I	II	(10^{24} cm^{-2})	I	II	HB	HDSB	
SMM 1/FIRS 1	71	46	84	250	900	1.3	2.2	6	3	5.2	
SMM 2	10	6	0.8–32	170	970	0.7	0.3	2.3	0.6		Extended
SMM 3	18	8	2–32	170	1000	0.7	0.6	4	0.9	1.8	
SMM 4	16	9	3–32	270	1400	1.5	1.2	6	3	3.2	
SMM 9/S 68N	16	6		160	1200	0.6	1.7	5	1.0		

References: LLM = This paper, HB = Hurt & Barsony (1996), CED = Casali et al. (1993), I = Single temperature/optically thin approximation, II = Radiative transfer model, HDSB = Hogerheijde et al. (1999).

† All reduced to the same distance, viz. $d = 310$ pc. Our luminosities refer to 40–3 000 μm.

$^\pounds$ Opacities from Ossenkopf & Henning (1994: MRN with thin ice mantles, 10^7 cm^{-3} and 10^5 yr, for which $\beta = 1.8$).

‡ Refers to I (single temperature, optically thin approximation).

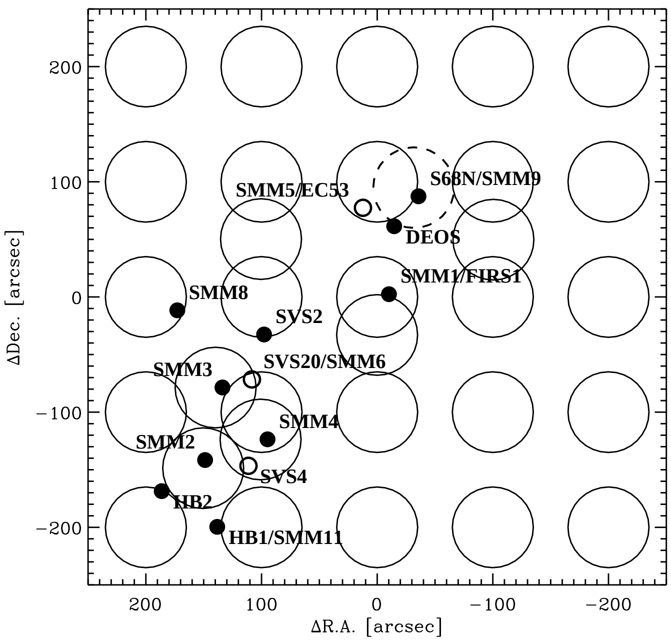

Fig. 10. The positions observed with the LWS and those of the sources included in the *Maximum Likelihood Method* deconvolution. Solid circles correspond to the LWS beams and the dashed circle especially marks an LWS observation, which is taken at a different time than the grid points in the map (see Sect 4.2.3). The filled dots refer to the FIR/sub-mm sources for which the deconvolution computations were performed - in the wavelength range 50 to 200 μm - whereas the small open rings identify sources which were omitted in the final FIR point source modelling (see the text)

spectral bins were treated as independent observations, so that the fact that the resulting SEDs are continuous and have a meaningful appearance, lends confidence in the method. There is no a priori reason that this should be the case (cf. Eqs. A1 to A9). However, confirmation must ultimately come from direct observation. With this proviso in mind, the results of these deconvolution computations are examined for individual sources in subsequent sections.

4.2.2. Spectro-spatial deconvolution results: the south-eastern sources

In the south-east part of the map, the level of confusion is high, with many sources contributing to the observed emission. A few sources are however dominant, viz. in the near infrared SMM 6/SVS 20 and at submillimetre wavelengths SMM 3 and SMM 4, respectively.

SMM 2, 3 and 4: Satisfactory solutions were obtained for the sources SMM 3 and SMM 4, whereas the broad spectrum of SMM 2 cannot plausibly be represented by a modified single-temperature blackbody (see Fig. 11). This is consistent with the interferometric observations by Hogerheijde et al. (1999) and by Choi et al. (1999), which failed to reveal a central condensation for SMM 2. Kaas (1999) found a K-band nebulosity at this position. We interpret its LWS spectrum therefore to be that of an extended structure.

Dust temperatures of SMM 2–4 are of the order of 30 K (Table 2), which is in general agreement with earlier work (Harvey et al. 1984), but which again contrasts to the lower values obtained by Hurt & Barsony (1996). Also the extent of the FIR photospheres is considerably smaller, on the order of a few arcsec rather than ten arcsec. For these optically thick envelopes (Table 2) the masses, which are in the range 2 to 6 $M_\odot$, would be severly underestimated by the optically thin approximations (Table 3).

SVS 2, SVS 4 and SMM 6/SVS 20: The point source assumption leads immediately to inconsistencies for SVS 2, which would become unreasonably bright in the far infrared, which is highly unlikely given the non-detection of the source at longer wavelengths (Fig. 12). An overall better solution is obtained for an extended source, filling the LWS beam. The modelling by Hurt & Barsony (1996) gave a very different picture, which yielded three nearly equally strong FIR point sources, with SVS 2 being only slightly stronger at 100 μm.

The modelling results in largely undetectable LWS fluxes for SVS 4 and SVS 20. In particular for SVS 4, these low flux levels are consistent with the lack of detection at 3 mm, whereas

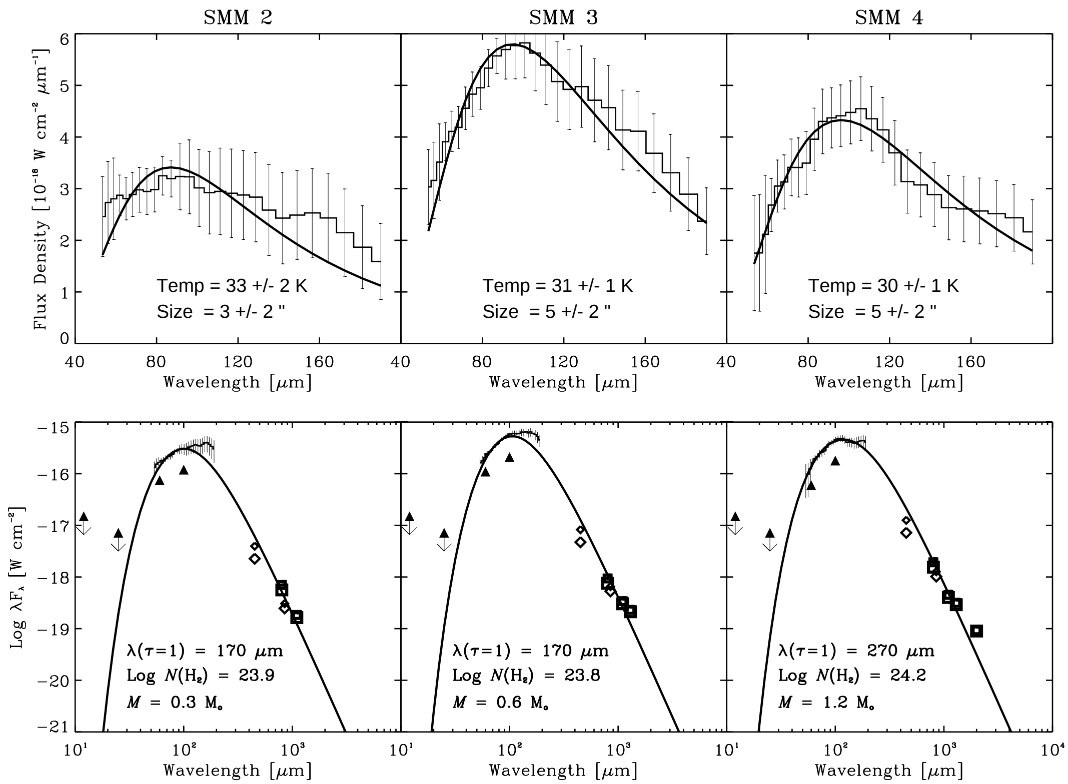

Fig. 11. Upper panels: The LWS spectra of SMM 2, SMM 3 and SMM 4, which are the results of the spectro-spatial deconvolution technique described in the text. The solid lines illustrate the blackbody fits to the data which are shown as histograms. The error-bars are given by (cf. Appendix A): $\Delta F_S = \sum \Omega\, \Delta F_M / \sum \Omega$, where $\Delta F_M = \Delta F_O + \mid F_O - \sum \Omega\, F_S \mid$ and where ΔF_O are the errors displayed in Fig. 2. **Lower panels:** Modified blackbody fits over the full SED range (10 – 10^3 μm). Literature and/or ISO data are coded as in Fig. 5

for SVS 20 some emission is possibly present at the shortest LWS wavelengths. The objects of this group are clearly visible at near infrared wavelengths, as stellar clusters and nebulosity and in Table 2, these objects are therefore identified as NIR sources. Further, our solutions for the LWS data provide reasonable complements to the CVF data (see Fig. 12), which have been obtained at the considerably higher spatial resolution of 6″ and, hence, are as such not dependent on any models.

SMM 8, SMM 11/HB 1 and HB 2: These sources represent the fainter members of the south-eastern group in the Serpens cloud core. The objects designated PS (Point Source) by Hurt & Barsony (1996) are labelled HB 1 and HB 2 in Figs. 10 and 13. Whereas the algorithm finds reasonable solutions for SMM 8 and HB 2, identifying them as point sources of roughly 5″ size at $T \gtrsim 20$ K, it fails for SMM 11/HB 1. At that location, Kaas (1999) recently found a source at 2 μm.

4.2.3. Spectro-spatial deconvolution results: the north-western sources

The members of this group, north of SMM 1, include SMM 9/S 68N, SMM 5 and DEOS, the ‘Deeply Embedded Outburst Star’ of Hodapp et al. (1996). As previously pointed out, the strong FIR source SMM 1 is comfortably displaced from the other three sources, the LWS data of which are quite severely confused (see Fig. 10). These confusion problems have also been encountered by Hurt & Barsony (1996), who divided the total flux into three equal parts among these objects.

SMM 5 and SMM 9/S 68N: At the position of SMM 5, no recognisable point source was found at LWS wavelengths (Fig. 14). The object coincides with a bow-shock shaped nebula and it could be that no well defined pre-stellar condensation exists. On the other hand, it is quite likely that SMM 5 simply is relatively too weak to be detectable. In order not to unnecessarily increase the noise, the source was excluded from further modelling.

Towards the S 68N complex, two independent LWS observations exist: one is a pointed observation, the other a grid point in our map. Spatially, these two observations are separated by about half a beamwidth (33″), and temporally, by about half a year (Table 1). The difference in flux amounts to about a factor of two, as would be expected, if S 68N solely would dominate the FIR emission in this region. The observations by Davis et al. (1999) revealed SMM 9/S 68N to be the dominant submm source, by factors of about 2–3 in flux. We expect, therefore, this source to be the brightest also in the far infrared, i.e. at the *longest* LWS wavelengths. This seems indeed to be the case, as shown in Fig. 14, where the modelling reveals a relatively cool source ($T \gtrsim 20$ K).

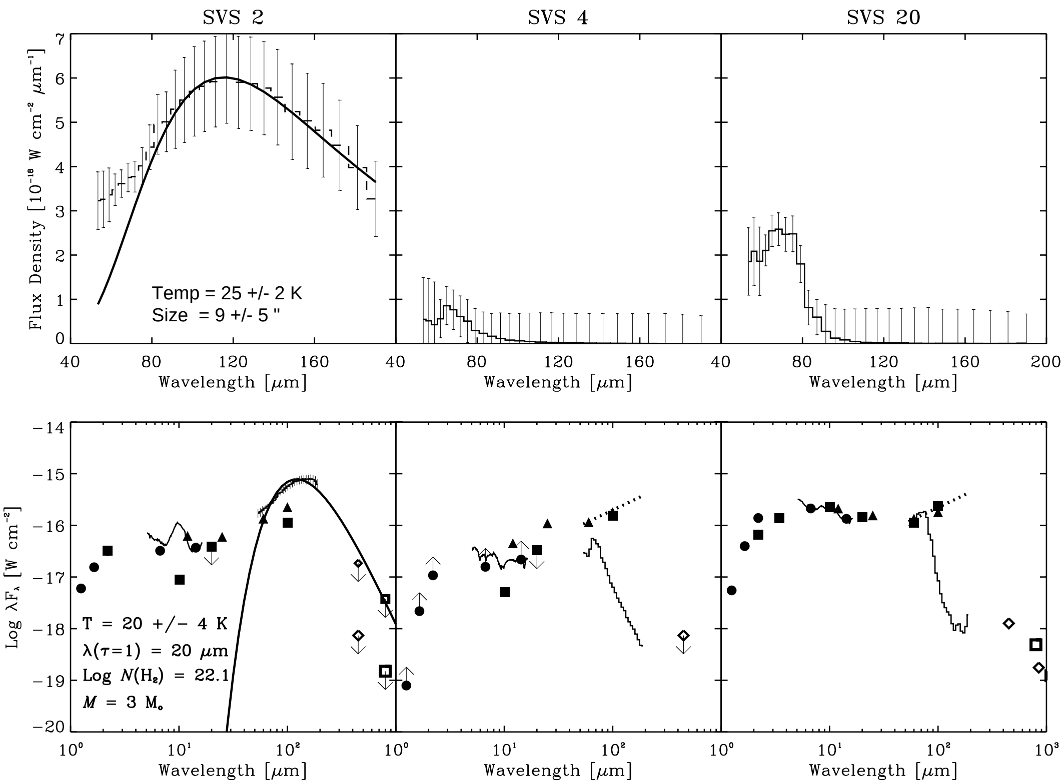

Fig. 12. Same as Fig. 11 but for SVS 2, SVS 4 and SMM 6/SVS 20. SVS 2 is actually better modelled as extended emission in the far-infrared. This is shown in the panel below by the larger upper limits in the submillimetre, which refer to a source filling the LWS beam. For SVS 4 and SVS 20, the dotted lines in the lower panels depict the deduced $3\,\sigma$ upper limits on the flux λF_λ in the LWS regime

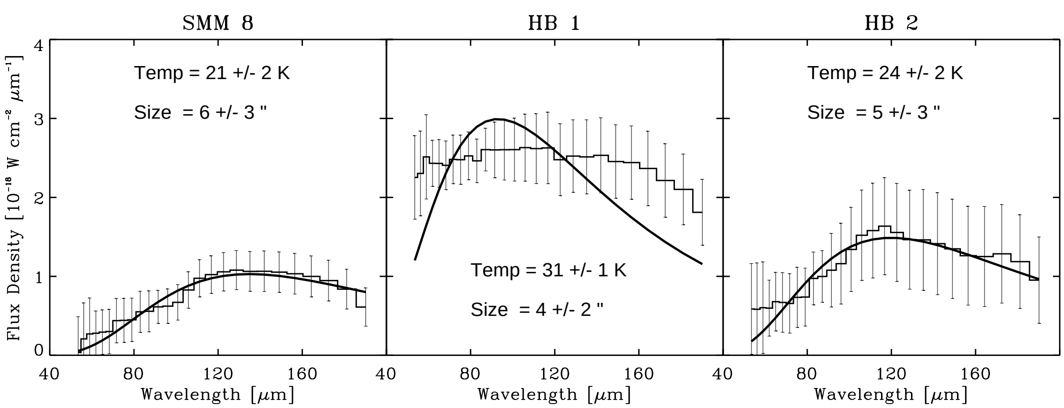

Fig. 13. Similar as Fig. 11 but for SMM 8, HB 1 and HB 2, except that only the upper panels have been included

DEOS: A further underlying assumption of our deconvolution method is that the emission does not vary with time. This was previously taken tacitly for granted, since this condition is normally fulfilled in the far infrared. For the outburst source DEOS, there is a potential risk, however, that this may not apply. Between August 1994 and July 1995, this object had increased its brightness by almost 5 mag in the K-band (Hodapp et al. 1996).

At near to midinfrared wavelengths, DEOS was observed, during about one year and a half, by T. Prusti with the SWS on six different dates (see Table 1: April 14, 1996, to October 22, 1997). The time evolution of the short-wave SED is displayed in Fig. 15, from which it is evident that, between April and October 1996, the SWS flux had dropped by a factor of two. This is remarkably similar to what happened to the (quasi-)simultaneous LWS spectra and led us to suspect that some or most of the FIR flux in fact was due to DEOS rather than to SMM 9, as might have been concluded on the basis of the discussion in the previous paragraph.

Fortunately, the possibility exists to check the temporal behaviour of the SWS data with independent ISOCAM observations (see Table 4). We performed aperture photometry on CAM images, which were obtained in two broad-band filters centred on ~ 7 (LW 2) and 15 μm (LW 3), respectively. These observations were performed when DEOS was both in the SWS-high (April

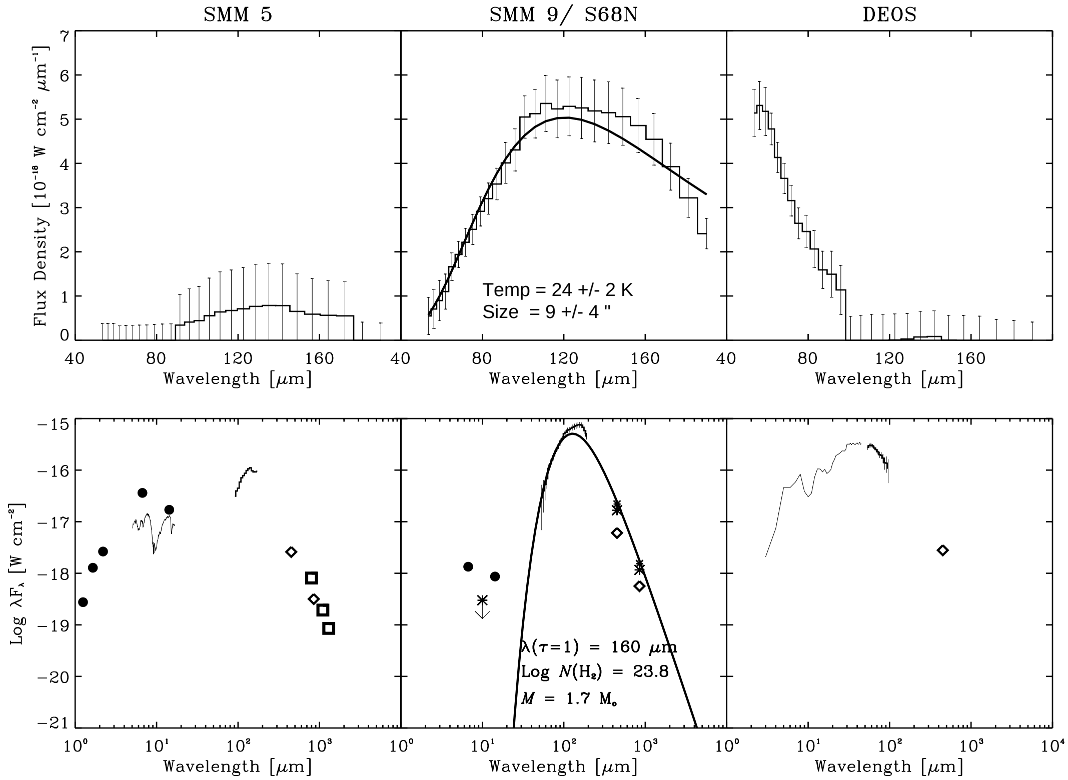

Fig. 14. Same as Fig. 11 but for SMM 5, SMM 9/S 68N and DEOS. The data shown by the asterisks in the SED of SMM 9/S 68N are from Wolf-Chase et al. (1998)

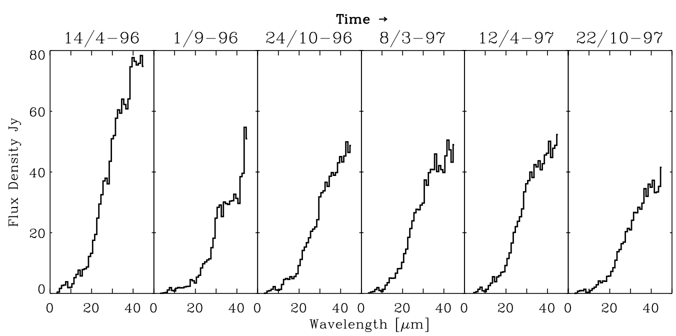

Fig. 15. Time evolution of the shortwave SED of DEOS, obtained with the SWS in the wavelength interval 2–45 μm. After April 14, 1996, the spectral flux density had decreased by a factor of about two and then stayed constant until the last measurement, i.e. October 22, 1997

Table 4. Aperture photometry in ISOCAM images in Jy/beam, where the beam is that of the SWS

Object	Filter	14 Apr 96	22 Sep 97	Ratio
DEOS	LW 2	2.8	2.2	1.27
DEOS	LW 3	6.8	5.4	1.26
EC 53	LW 2	0.90	0.90	1.00
EC 53	LW 3	1.12	1.15	0.97

14, 1996) and in the SWS-low state (September 22, 1997). Table 4 summarises the photometry results for DEOS and a reference star (EC 53), expressed in Jy/beam, where the ‘per beam’ refers to the aperture size of the SWS. Evidently, the CAM data also reveal significant variability for DEOS, by a factor of about 1.3 in both filters. At 7 μm, the SWS spectra are too noisy to be meaningfully measured, but the SWS data in the 15 μm region are in excellent agreement with the CAM-value.

In conclusion, the evidence presented firmly establishes that DEOS had changed its flux in the near- to mid-infrared between April and October, 1996. It seems very likely therefore that also the LWS spectra show traces of this variability. In this context we recall that in the submillimetre SMM 9/S 68N is the strongest source. Hence, it seems very likely that, at the time of the LWS observations in October 1996, DEOS was not dominant at the longest wavelengths, but might have contributed significantly at the shorter LWS wavelengths. A longwave fit for S 68N to the pointed LWS observation was properly scaled and subtracted and the spectro-spatial deconvolution modelling was done for the residual. This led finally to the solutions for the SEDs of DEOS presented in Fig. 16.

The joining of the *observed* SWS and *modelled* LWS spectra for both the high and the low state is quite spectacular. This indicates that the algorithm we have used is indeed capable of providing satisfactory results. We suggest therefore that the spectra presented in Fig. 16 represent the most likely SEDs for the outburst source DEOS. As far as we are aware, these would be seen for the first time and should be helpful in constraining outburst models and, perhaps, in differentiating source type (e.g. FUOR vs non-FUOR or EXOR). The far-infrared SEDs of FUORs appear very different though (Fig. 17).

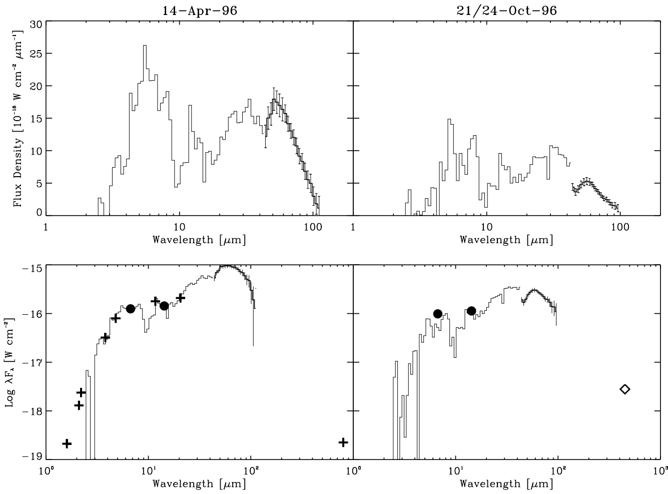

Fig. 16. SEDs of DEOS in high (left) and low state (right), referring to the dates shown above the frames. The SWS parts of the data have been directly observed, whereas the LWS branches result from the spectro-spatial deconvolution modelling. Plus-signs refer to data by Hodapp et al. (1996), and are thus not simultaneous with the ISO data, and filled circles to the ISOCAM data presented in Table 4; other symbols are as in Fig. 5. The SEDs contain considerable spectral structure. Using the calibration by Whittet (1998) the optical depth of the silicate feature at 10 μm, $\tau_{9.7} \sim 1.3$, would implicate some 20 magnitudes of visual extinction to the continuum source

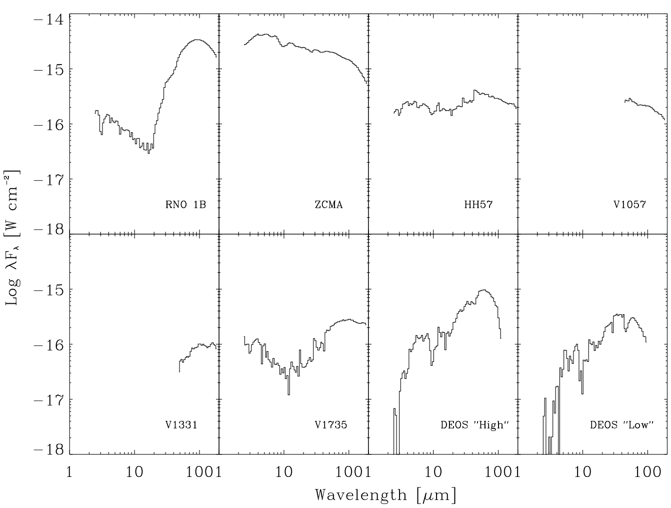

Fig. 17. ISO observations of FUORs resulted in the infrared SEDs of RNO 1B, Z CMa, HH 57, V 1057 Cyg, V 1331 Cyg and V 1735 Cyg. For reference the SEDs of DEOS are shown to scale

4.3. Summarising discussion

Tables 2 and 3 summarise the results of the LWS observations and our spectro-spatial deconvolution modelling. For cool sources, the good wavelength coverage and resolution of the LWS is generally better adapted to estimate the temperature than the poor resolution and short range of IRAS data. The source emission is generally optically thick in the LWS spectral range. Compared to the estimates based on IRAS data by Hurt & Barsony (1996) our temperatures of the SMM sources are generally higher, indicative of a larger number of photons heating the dust. This is also effectively expressed by our larger luminosities, although the derived sizes of the FIR photospheres (e.g., $\tau_{100\mu m} \sim 1$) are generally smaller than the dimensions obtained by Hurt & Barsony (1996).

We have deduced the observed β values from the slopes of the Rayleigh-Jeans part of the source SEDs and obtain generally quite shallow distributions, viz. $|\beta| \leq 1$. This is in line with the findings by, e.g., Casali et al. (1993), Testi & Sargent (1998) and Davis et al. (1999). However, for a given source, the scatter among different observations is large and it appears doubtful that β could be a useful diagnostic for SMM-type objects. In fact, the observed flatness probably indicates that the assumption of optically thin emission is not valid. This hypothesis is supported by detailed radiative transfer models, in which the temperature distribution is self-consistently calculated. Models were calculated for five sources, for which sufficient data were available, viz. SMM 1, 2, 3, 4 and 9. These models are optically thick out to millimetre wavelengths and envelope masses are in the range 2–6 $M_{\odot}$.

The luminosities of these SMMs are in the range 10–70 $L_{\odot}$. Much or most of this luminosity is presumably produced by mass accretion processes. These depend on the centrally accumulated mass. It is at present difficult to tell whether the SMMs will end up on the main sequence as low-mass or as intermediate mass stars ($\lesssim$ 1–3 $M_{\odot}$; the distance too comes in here as a crucial parameter). As OH and/or H_2O masers normally are found towards young sources of higher mass, the detection of such emission towards SMM 1 by Rodríguez et al. (1989) and Curiel et al. (1993), respectively, would speak in favour of the intermediate mass option, at least for that object. In any case, the existence of these massive envelopes around the SMMs argues for the idea that these sources are in a very early stage of their development. One can also speculate that most of these massive envelopes will have become dispersed on a relatively short timescale ($\sim 10^5$ yr).

5. Conclusions

The main conclusions of this work can be summarised as follows:

- In order to disentangle the contribution of individual sources to the FIR emission in a $8' \times 8'$ map obtained with the ISO-LWS a *Maximum Likelihood Method* is introduced. This spectro-spatial deconvolution technique enabled us to restore the FIR spectra (50 to 200 μm) of previously known submillimetre sources (SMMs).
- Observations of SMMs with the LWS are advantagous as the data sample the peak of the spectral energy distributions (SEDs). This permits an accurate determination of the dust temperatures. These temperatures are generally found to be higher than those obtained from high resolution IRAS data.
- Fits to the observed SEDs by modified blackbodies reveal that the SMMs are generally optically thick at LWS wavelengths.

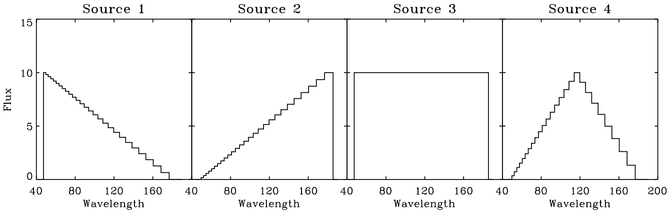

Fig. B.1. The FIR spectra of the four point sources included in the test example have simple forms in the wavelength range of the LWS observations. The binning corresponds, as before, to $R_\lambda = 20$

- In addition, for reasonable assumptions about the grain opacities, the Rayleigh-Jeans part of the observed SEDs is significantly flatter than what would be expected for optically thin dust emission. We interpret this to indicate the SMMs to be optically thick out too much longer wavelengths than previously assumed.
- Self-consistent radiative transfer calculations confirm the correctness of this assertion. These models of the SMMs are optically thick out to mm-wavelengths. These dust envelopes are massive, several $M_\odot$, suggesting that these sources are still in their very infancy.
- The outburst source DEOS has been observed with various instruments aboard ISO and at different times. The source had certainly varied in infrared brightness and we present the full infrared spectra, at both high and low states, for the first time.

Acknowledgements. We wish to thank the referee, N.J. Evans II, for valuable suggestions which led to improvements of the manuscript. The authors from the Stockholm Observatory acknowledge the support by the Swedish National Space Board.

Appendix A: spectro-spatial deconvolution: the algorithm

The aim of the presented algorithm is to restore the SEDs of sources in a crowded field. To be able to handle spatially undersampled and noisy spectroscopic data we developed a program based on the *Maximum Likelihood Method* (e.g., Lucy 1974). The present discussion is based on our LWS observations, but the method per se should of course be more widely applicable.

The first of two basic assumptions is that all sources are point-like, which is probably reasonable considering the large beam size of the LWS (HPBW $\sim 70''$). Secondly, the exact positions of all sources are assumed known and kept fixed. We then pick an arbitary grid point within the field of the LWS-map and try to estimate, at that location and for a fixed frequency, the radiative flux which originated from all sources in the field. This is done at all locations and for all LWS wavelengths in an iterative scheme as described in the following.

The photon distribution can be assumed to follow Poisson statistics and, hence, the probability to observe O_m detector counts at the position m can be written as

$$P_m = \frac{e^{-E_m}\, E_m^{O_m}}{O_m!} \tag{A.1}$$

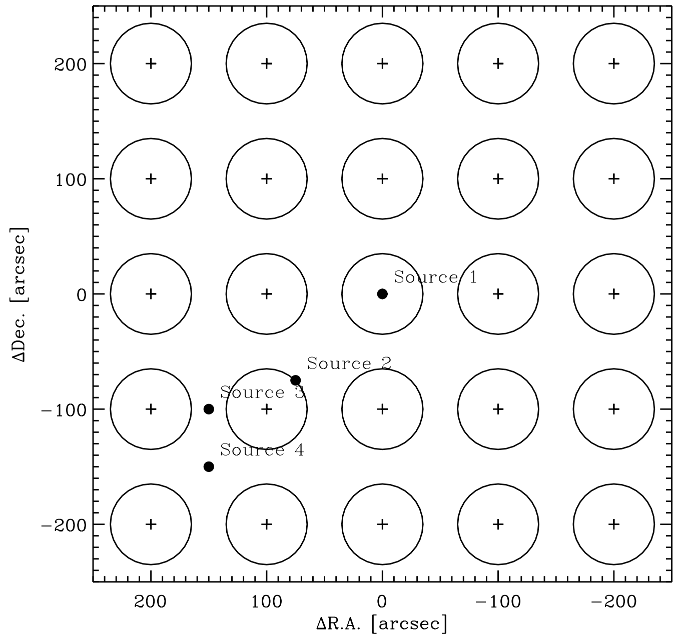

Fig. B.2. Map showing the grid points of the simulated observation, the HPBW of the LWS and the positions of the point sources 1 to 4 having the spectra shown in Fig. B.1

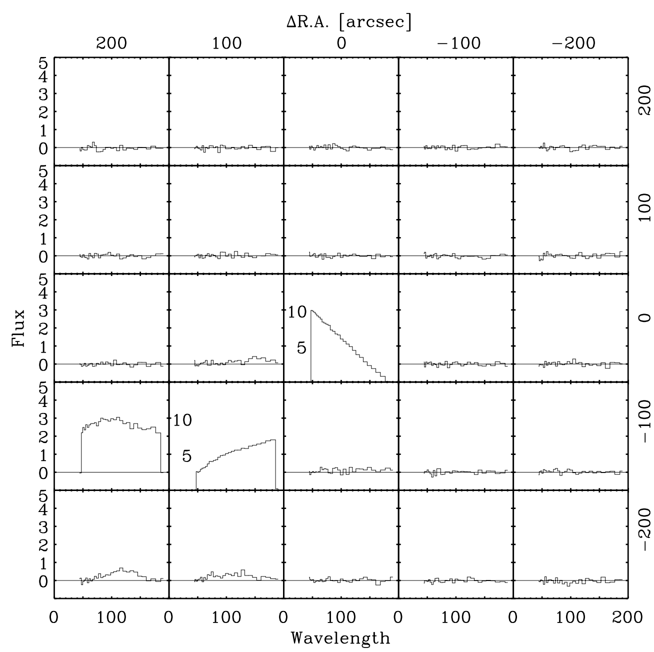

Fig. B.3. The simulated observation of sources 1 to 4 (with added noise) results in the shown undersampled LWS map of spectra (cf. Fig. 2). Notice in particular the very faint and noisy appearance of source 4

where

$$E_m = \sum_{s=1}^{N_S} \Omega_{m,s}\, S_s \tag{A.2}$$

is the expected number of counts at position m, arriving from N_S sources, each contributing S_s counts and being at positions s. $\Omega_{m,s}$ is the diffraction pattern of the instrument (the 'beam',

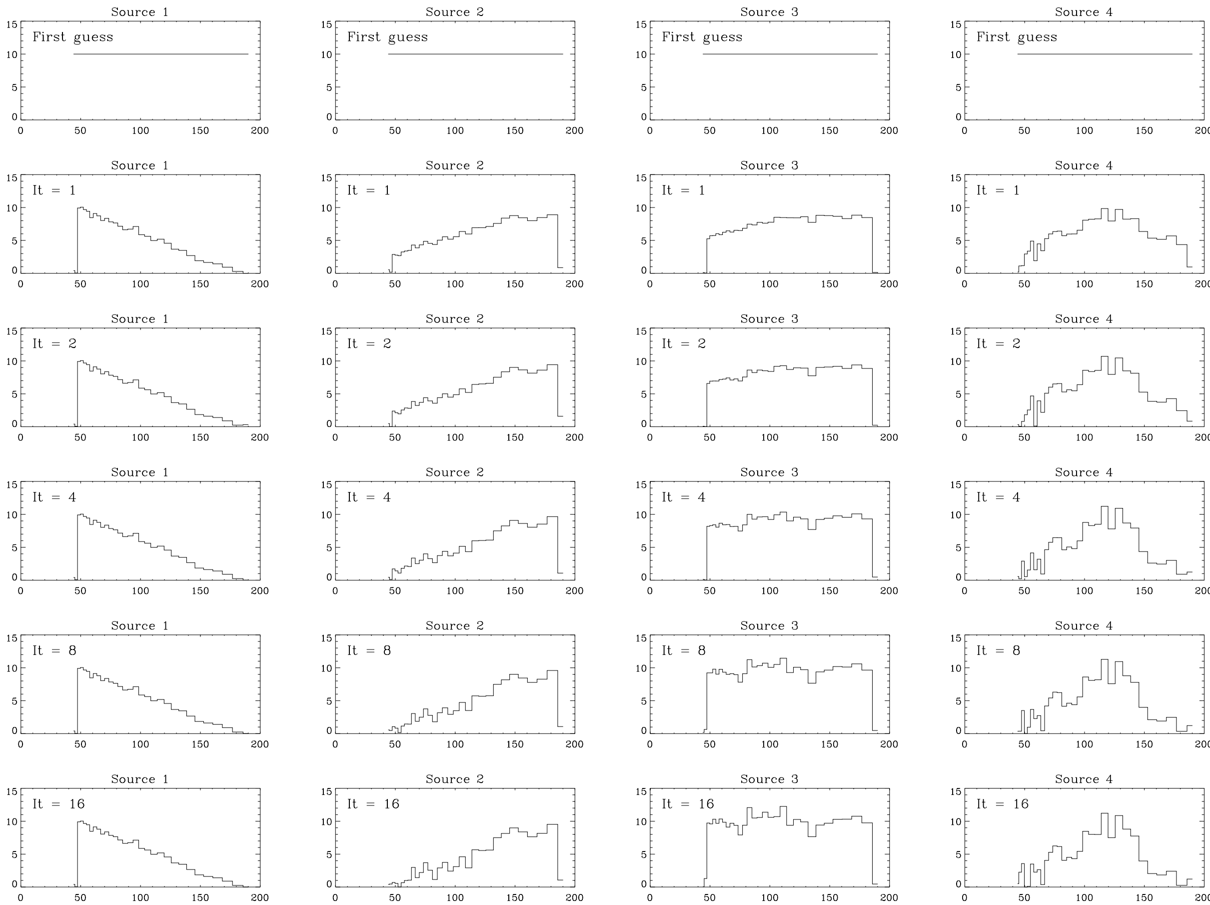

Fig. B.4. The iterative spectro-spatial deconvolution process is shown vertically for the sources 1 to 4, from left to right. The first row shows the start conditions for the source spectra, viz. simply a constant spectral distribution. Convergence is achieved already after four iterations, shown in the fourth row. Iterating further does not improve on the results: see rows 5 and 6, showing the results after 8 and 16 iterations, respectively

see Fig. 9). Designating the likelihood to observe the counts from a map containing N_M points by

$$L = P_1\, P_2\, P_3\, \cdots\, P_{N_M} \tag{A.3}$$

one can also write

$$\ln L = \sum_{m=1}^{N_M} O_m \ln E_m - E_m - \ln O_m! \tag{A.4}$$

Solving for the maximum likelihood, viz.

$$\frac{\partial \ln L}{\partial S_s} = 0 \tag{A.5}$$

for all positions s, or

$$\sum_{m=1}^{N_M} \Omega_{m,s}\, \frac{O_m}{E_m} = \sum_{m=1}^{N_M} \Omega_{m,s} \tag{A.6}$$

From the last expression, a correction factor can be obtained

$$C_s = \frac{\sum_{m=1}^{N_M} \Omega_{m,s} \frac{F_m^O}{F_m^M}}{\sum_{m=1}^{N_M} \Omega_{m,s}} \tag{A.7}$$

where F_m^O is now the observed flux (for a linear detector) at position m and where

$$F_m^M = \sum_{s=1}^{N_S} \Omega_{m,s}\, F_s^S \tag{A.8}$$

is the expected flux at this position, originating from N_S sources at positions s and contributing the flux F_s^S. Finally, the iteration is then

$$F_s^S\,(New) = C_s F_s^S\,(Old) \tag{A.9}$$

for all wavelengths λ, yielding the source spectra.

Appendix B: spectro-spatial deconvolution: test

As an example of a test case, an observation of the LWS map was simulated. We chose four FIR spectra, the shape of which is described by simple geometric figures (positive ramp, negative ramp, rectangular box and triangle: see Fig. B.1). The point-like sources of these spectra were distributed on the LWS grid in the manner depicted in Fig. B.2, i.e. source 1 centred on a grid point (which therefore should not be affected by the convolution, but still by the noise), source 2 on the half-power contour of the

LWS beam, source 3 situated half-way between two grid points and source 4 farthest away from any grid point.

At each wavelength (spectral resolution $R_\lambda = 20$) for every map position the sources were convolved with the LWS beam of Fig. 9 and (white) noise was added. This results in the simulated observations shown in Fig. B.3. These “observed” maps (one per spectral bin) were then run thrugh the *Maximum Likelihood* algorithm for a number of iterations.

The result of the deconvolution is shown in Fig. B.4, where the succession of iterations is ordered vertically for each of the four sources. The first row shows the start conditions, where we “guessed” a simple constant spectrum in all cases. These straight line spectra have changed to resemble the true source spectra already after the first run. In this particular test case, the deconvolutions have converged after about 4 iterations (fourth row), i.e. successive iterations do not give further improvements. Apparently, the spectra of particularly source 1, as expected, but also of sources 2 and 3 are very well reproduced. The most difficult test case is source 4 (cf also Fig. B.3), which is located farthest away from the map points, and therefore considerably more affected by the noise. Nevertheless, our method reproduced its spectrum reasonably well too.

We conclude that this test procedure was successful, which lends credibility to the reliability and potential of the developed spectro-spatial deconvolution algorithm.

References

André P., Ward-Thompson D., Barsony M., 1993, ApJ 406, 122
Bohlin R.C., Savage B.D., Drake J.F., 1978, ApJ 224, 132
Bontemps S., Nordh L., Olofsson G., et al., 2000, preprint
Casali M.M., Eiroa C., Duncan W.D., 1993, A&A 275, 195
Cesarsky C.J., Abergel A., Agnèse P., et al., 1996, A&A 315, L 32
Choi M., Panis J.-F., Evans II N.J., 1999, ApJS 122, 519
Clegg P.E., Ade P.A.R., Armand C., et al., 1996, A&A 315, L 38
Curiel S., Rodríguez L.F., Moran J.M., Cantó J., 1993, ApJ 415, 191
Curiel S., Rodríguez L.F., Gómez J.F., et al., 1996, ApJ 456, 677
Davis C.J., Matthews H.E., Ray T.P., Dent W.R.F., Richer J.S., 1999, MNRAS 309, 141
Emerson J.P., 1988, In: Dupree A.K., Lago M.T.V.T. (eds.) Formation and Evolution of Low Mass Stars. Kluwer Acad. Pub., p. 21
de Graauw Th., Haser L.N., Beintema D.A., et al., 1996, A&A 315, L 49
de Lara E., Chavarria-K. C., López-Molina G., 1991, A&A 243, 139
Harvey P.M., Wilking B.A., Joy M., 1984, ApJ 278, 156
Hildebrand R.H., 1983, QJRAS 14, 267
Hodapp K.-W., Hora J.L., Rayner J.T., Pickles A.J., Ladd E.F., 1996, ApJ 468, 861
Hogerheijde M.R., van Dishoeck E.F., Salverda J.M., Blake G.A., 1999, ApJ 513, 350
Hurt R.L., Barsony M., 1996, ApJ 460, L45
Kaas A.A., 1999, Ph.D. Thesis, Stockholm University
Kessler M.F., Steinz J.A., Anderegg M.E., et al., 1996, A&A 315, L 27
Lucy L.B., 1974, AJ 79, 745
McMullin J.P., Mundy L.G., Wilking B.A., Hezel T., Blake G.A., 1994, ApJ 424, 222
Nordh L., van Duinen R.J., Sargent A.I., et al., 1982, A&A 115, 308
Ossenkopf V., Henning Th., 1994, A&A 291, 943
Rieke G.H., Lebofsky M.J., 1985, ApJ 288, 618
Rodríguez L.F., Curiel S., Moran J.M., et al., 1989, ApJ 34, L 85
Savage B.D., Mathis J.S.,, 1979, ARA&A 17, 73
Swinyard B.M., Clegg P.E., Ade P.A.R., et al., 1996, A&A 315, L 43
Testi L., Sargent A.I., 1998, ApJ 508, L 91
White G.J., Casali M.M., Eiroa C., 1995, A&A 298, 594
Whittet D.C.B., 1998, In: Dust in the Universe
Wolf-Chase G.A., Barsony M., Wootten H.A., et al., 1998, ApJ 501, L 193
Ziener R., Eislöffel J., 1999, A&A 347, 565